Faraday Discussions

Accepted Manuscript

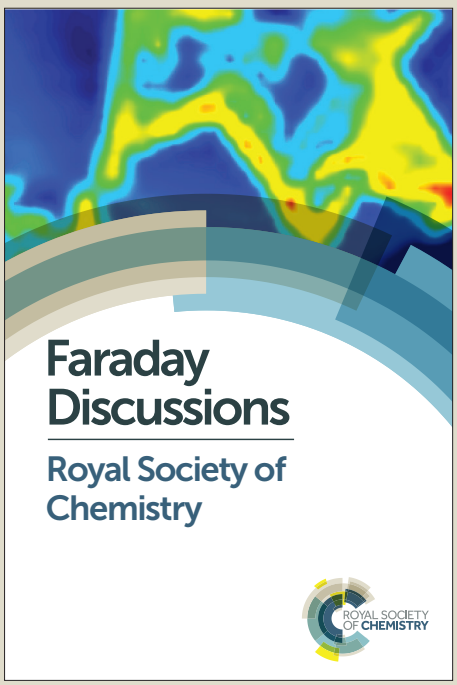

This article can be cited before page numbers have been issued, to do this please use: J. Suchan, D. Hollas, B. Curchod and P. Slavicek, *Faraday Discuss.*, 2018, DOI: 10.1039/C8FD00088C.

View Article Online
DOI: 10.1039/C8FD00088C

On the Importance of Initial Conditions for Excited-State Dynamics

Jiří Suchan,[1] Daniel Hollas,[1] Basile F. E. Curchod,[2] and Petr Slavíček,[1]*

[1] *Department of Physical Chemistry, University of Chemistry and Technology, Prague, Technická 5, 16628 Prague, Czech Republic*

[2] *Department of Chemistry, Durham University, South Road, Durham DH1 3LE, United Kingdom*

*Corresponding authors: petr.slavicek@vscht.cz

Abstract

Photodynamical simulations are increasingly used for exploring photochemical mechanisms and interpreting laser experiments. The vast majority of *ab initio* excited-state simulations are performed within semiclassical, trajectory-based approaches. Apart from the underlying electronic-structure theory, the reliability of the simulations is controlled by a selection of initial conditions for the classical trajectories. We discuss appropriate choices of initial conditions for simulations of different experimental arrangements: dynamics initiated by continuum-wave (CW) laser fields or triggered by ultrashort laser pulses. We introduce a new technique, CW-sampling, to treat the former case, based on the ideas of importance sampling, combined with the quantum thermostat approach based on the Generalized Langevin Equation (GLE) that allows for an efficient sampling of both position and momentum space. The CW-sampling is particularly important for photodynamical processes initiated by absorption at the tail of the UV absorption spectrum. We also emphasize the importance of non-Condon effects for the dynamics. We demonstrate the performance of our approach on the photodissociation of the CF_2Cl_2 molecule (freon CFC-12). A quantitative agreement with the experimental data is achieved with the use of empirical correlation energy correction (CEC) factor on top of FOMO-CASCI potential energy surfaces.

View Article Online
DOI: 10.1039/C8FD00088C

Introduction

Computational methods contribute a great deal to the understanding of photochemical mechanisms, interpretation of laser spectroscopy experiments, and quantitative simulations of photochemical parameters. *Ab initio* theories provide an insight into photochemistry primarily by mapping potential energy surfaces[1] (PESs), but direct dynamical simulations in the excited states have become almost routinely used as well[2,3]. Explicit integration of equations of motion provide reaction yields, timescales, and mechanisms. *Ab initio* molecular dynamics, with forces calculated on-the-fly, became popular as no prior knowledge or intuition on the processes under study is needed: the dynamics itself leads us to the important parts of phase space. In the last decade, *ab initio* photodynamics has gradually become a mature field due to both methodological developments and ever increasing computational power – for example, the introduction of graphical processing computations allowed for excited-state calculations with hundreds of atoms[4].

Most of *ab initio* excited-state simulations are in some way based on trajectories, as quantum chemical codes provide us only with the local description of the potential energy surface. While the trajectory-based simulations are of classical nature, the nuclear quantum effects must be accounted for at least to some extent. First, we often need to treat coupled electron/nuclear dynamics as the failure of Born-Oppenheimer approximation is more a rule rather than an exception in the excited-state dynamics. Various schemes for treating nonadiabatic transitions are used, ranging from semiclassical schemes such as Ehrenfest dynamics, modified Landau-Zener approach[5] or surface hopping[6,7] to more "quantum" schemes such as the Full Multiple Spawning method[8–10], variational multi-configuration Gaussian wavepackets[11,12], or the coupled-trajectory mixed quantum/classical method[13].

Another nuclear quantum effect to consider is the ground-state vibrational delocalization of atomic nuclei. This relates to an important yet often underrated question: How to properly choose initial conditions for semiclassical calculations? In other words, how should we select the set of positions and momenta for each of the atoms in the system so that they correspond to the actual experimental setup?[14] We argue in the present work that performing molecular dynamics with the so called "quantum thermostat" approach[15] represents a convenient way to sample the initial state of a quantum system in thermal equilibrium. The initial conditions should be, however, different for experiments with ultrashort light pulses forming a wavepacket in the excited state than for experiments employing continuum wave (CW) laser field. Majority of the present day photodynamical simulations assumes the system to be

View Article Online
DOI: 10.1039/C8FD00088C

vertically promoted into an excited state, forming a vibrational wavepacket, which is then treated within a semiclassical framework. This view corresponds to an excitation *via* an ultrashort laser pulse. Experimentally, this assumption is typically not fulfilled. Most experiments are performed with photons of fixed energy - nanosecond lasers and even shorter femtosecond laser pulses do not form vertical wavepackets. Hence, the interpretation of laser experiments requires different methods from those presently adopted by the community.

Vertical simulations does not allow for adequate treatment of wavelength dependent photochemical processes, as we encounter e.g. photochemistry of heterocycles[16], photolysis of glyoxal[17], photoinitiating reactions[18] or chemistry of phytochromophores[19] to name but few examples. Proper modeling of molecules interacting with fixed wavelength light is critical for a quantitative modeling of photochemical reactions. Let us consider a photochemical rate constant

$$j = \int_{\lambda_i}^{\lambda_j} \sigma_a(\lambda)\phi_a(\lambda)I(\lambda)d\lambda. \quad (1)$$

Knowing the photon flux for each wavelength $I(\lambda)$, we need to calculate the absolute absorption cross section σ_a and quantum yield ϕ_a of a selected reaction channel for a wavelength λ. Such a task is of uttermost importance e.g. in atmospheric chemistry or astrochemistry where the important species are often difficult to characterize experimentally due to their transient character or difficult experimental realization such is the case of aerosols. Both the cross sections and the quantum yields can be calculated from an ensemble of structures obtained from semiclassical dynamical simulations. Here, we encounter the problem of calculating the quantum yield (or any other dynamical quantity of interest) for a given wavelength. Unlike in computational spectroscopy[20], the field of computational photodynamics has not quite reached the level of accuracy at which the tools would be interesting for the experimental or modeling community.

In the present study, we focus on the atmospherically important photodissociation of CF_2Cl_2 as a convenient test bed for the exploration of the fixed wavelength effects on the simulation results. The paper is organized as follows. We first discuss the theoretical foundation of photoexcitation processes, and then the simulation protocols used in the work – aiming at providing a general strategy for simulating different types of experiments within the framework of semiclassical simulations. We then provide technical details of our simulation

View Article Online
DOI: 10.1039/C8FD00088C

protocol and introduce the test system. Finally, we demonstrate the performance of the introduced methods in the result section.

Theory

Interaction of light with molecules: what states are formed?

Molecules, when excited by laser pulses, can end up in different quantum states depending on the pulse shape and phase structure. We begin by a short formal exploration of the states formed with a weak laser field, following the well-known perturbation theory treatment as pedagogically outlined e.g. by Persico[21]. In this framework, one defines a time-dependent perturbation $\hat{V}$ which, once applied onto an unperturbed system with set of eigenstates $|\Psi_j\rangle$, generates the time-dependent molecular wavefunction $|\Psi(\mathrm{t})\rangle = \sum_j c_j\,(t)|\Psi_j\rangle \exp(-iE_j t/\hbar)$. Here, E_j stands for the eigenvalue j of the unperturbed time-independent Schrödinger equation. Considering that only $|\Psi_0\rangle$ is populated initially, the perturbation is not too strong and we are interested only in the short-time evolution, the time derivatives of the expansion coefficients are given as:

$$\dot{c}_j = -\frac{i}{\hbar}\exp(i(E_j - E_0)t/\hbar)V_{j0}\,, \tag{2}$$

with $V_{j0} = \langle\Psi_j|\hat{V}|\Psi_0\rangle$. For a molecule in an external electromagnetic field we get in the dipole approximation $\hat{V} = -\hat{\boldsymbol{\mu}}\cdot\boldsymbol{\varepsilon}(t)$, containing the molecular dipole moment $\hat{\boldsymbol{\mu}}$ and the electric field $\boldsymbol{\varepsilon}(t)$, taken here as a linearly-polarized light pulse defined by $\boldsymbol{\varepsilon}(t) = \boldsymbol{\varepsilon}_0 A(t)\cos(\omega t)$. $A(t)$ is a time envelope for the pulse and $\boldsymbol{\varepsilon}_0$ is a constant vector given by $\boldsymbol{\varepsilon}_0 = \varepsilon_0\boldsymbol{\epsilon}$, where ε_0 is the maximum amplitude of the field and $\boldsymbol{\epsilon}$ a polarization vector. It then follows for time-dependent coefficients

$$\dot{c}_j = \frac{i}{\hbar}\exp\left(\frac{i\omega_{j0}t}{\hbar}\right)\boldsymbol{\mu}_{j0}\cdot\boldsymbol{\varepsilon}_0 A(t)\cos(\omega t)\,, \tag{3}$$

with $\boldsymbol{\mu}_{j0} = \langle\Psi_j|\hat{\boldsymbol{\mu}}|\Psi_0\rangle$. Upon integration of this equation from $t = -\infty$ to $t = \infty$, that is, from before the pulse starts to after it ends, we obtain

$$c_j(\infty) = \frac{i}{2\hbar}\boldsymbol{\mu}_{j0}\cdot\boldsymbol{\varepsilon}_0\int_{-\infty}^{\infty}\left(\exp\left(\frac{i(\omega_{j0}+\omega)t}{\hbar}\right) + \exp\left(\frac{i(\omega_{j0}-\omega)t}{\hbar}\right)\right)A(t)\,dt \tag{4}$$

View Article Online
DOI: 10.1039/C8FD00088C

$$= \frac{i\sqrt{\pi}}{\sqrt{2}\hbar}\boldsymbol{\mu}_{j0}\cdot\boldsymbol{\varepsilon}_0\left(\tilde{A}(-\omega-\omega_{j0})+\tilde{A}(\omega-\omega_{j0})\right).$$

We will further consider only excitation processes ($\tilde{A}(-\omega-\omega_{j0})=0$), so that we get

$$|\Psi\rangle = \frac{i}{\hbar}\sqrt{\frac{\pi}{2}}\sum_j |\Psi_j\rangle\boldsymbol{\mu}_{j0}\cdot\boldsymbol{\varepsilon}_0\tilde{A}(\omega-\omega_{j0})\,. \tag{5}$$

The Fourier transform of the time envelope, $\tilde{A}(\omega-\omega_{j0})$, encodes the distribution of frequency components of the laser pulse. $\tilde{A}(\omega-\omega_{j0})$ falls rapidly around $\tilde{A}(0)$ for a long pulse, *i.e.*, we get a narrow spectrum around the central frequency ω, whereas a very short laser pulse will be broad in the frequency domain.

Next, we focus our attention on a given electronic state, say the first electronic excited state $|\psi_1\rangle$, and will approximate each eigenstate $|\Psi_j\rangle$ as a vibronic state $|\psi_1\chi_{1u}\rangle$, where $|\chi_{1u}\rangle$ is the u^{th} vibrational state of the electronic state $|\psi_1\rangle$. We note at this stage that we neglect the interaction of the vibronic (bound) states of $|\psi_1\rangle$ with quasi-continuum or continuum vibrational states from a lower electronic state $|\psi_0\rangle$. The coupling between the initial (ground vibrational and electronic) state $|\psi_0\chi_{00}\rangle$ and the state $|\psi_1\chi_{1u}\rangle$ mediated by an external field is dictated by the transition dipole moment

$$\boldsymbol{\mu}_{1u,00} = \langle\psi_1\chi_{1u}|\hat{\boldsymbol{\mu}}|\psi_0\chi_{00}\rangle. \tag{6}$$

Equation (5) then turns into:

$$|\Psi\rangle \cong \frac{i}{\hbar}\sqrt{\frac{\pi}{2}}\sum_u \boldsymbol{\mu}_{1u,00}\cdot\boldsymbol{\varepsilon}_0|\psi_1\chi_{1u}\rangle\tilde{A}(\omega-\omega_{1u,00}). \tag{7}$$

This last equation constitutes our starting point to compare the effect of an ultrashort and a long laser pulse on a molecular system.

In the case of a long pulse of light, the term $\tilde{A}(\omega-\omega_{1u,00})$ will display a narrow peak centered around the pulse (almost monochromatic) frequency ω. Hence, if one considers that the separation between the vibrational states of $|\psi_1\rangle$ is large enough, the long pulse can select only one specific state $|\psi_1\chi_{1u}\rangle$ if its frequency is tuned to $\omega \approx \omega_{res} = (E_{1u}-E_{00})/\hbar$. As a result, the wavefunction turns into

View Article Online
DOI: 10.1039/C8FD00088C

$$|\Psi\rangle \approx \frac{i}{\hbar}\sqrt{\frac{\pi}{2}}\boldsymbol{\mu}_{1u,00}\cdot\boldsymbol{\varepsilon}_0\tilde{A}(\omega-\omega_{res})|\psi_1\chi_{1u}\rangle \tag{8}$$

Hence, the wavefunction generated by this laser pulse is simply proportional to the state $|\psi_1\chi_{1u}\rangle$, *i.e.*, we excite the molecule into one of its vibrational state in the excited electronic state (Fig. 1A).

Considering now an ultrashort laser pulse, its bandwidth is large enough to cover different vibrational states in the excited states, *i.e.*, $\tilde{A}\left(\omega-\omega_{1u,00}\right)$ in Eq. (7) is independent on the vibrational quantum number and replaced by the almost constant $\tilde{A}(\omega-\omega_{vert})$ term, where $\omega_{vert}=(E_1-E_0)/\hbar$ is the vertical excitation energy. In addition, we rewrite the transition dipole moment as $\boldsymbol{\mu}_{1u,00}=\langle\chi_{1u}|\langle\psi_1|\hat{\boldsymbol{\mu}}|\psi_0\rangle|\chi_{00}\rangle=\langle\chi_{1u}|\boldsymbol{\mu}_{10}^{e}|\chi_{00}\rangle$, with $\boldsymbol{\mu}_{10}^{e}(\boldsymbol{R})$ being the electronic transition dipole. Starting from Eq. (8), we obtain

$$\begin{aligned}
|\Psi\rangle &\cong \frac{i}{\hbar}\sqrt{\frac{\pi}{2}}\sum_u \boldsymbol{\mu}_{1u,00}\cdot\boldsymbol{\varepsilon}_0|\psi_1\chi_{1u}\rangle\tilde{A}\left(\omega-\omega_{1u,00}\right)\\
&\cong \frac{i}{\hbar}\sqrt{\frac{\pi}{2}}\tilde{A}(\omega-\omega_{vert})\sum_u |\psi_1\chi_{1u}\rangle\langle\chi_{1u}|\boldsymbol{\mu}_{10}^{e}\cdot\boldsymbol{\varepsilon}_0|\chi_{00}\rangle\\
&= \frac{i}{\hbar}\sqrt{\frac{\pi}{2}}\tilde{A}(\omega-\omega_{vert})\sum_u |\chi_{1u}\rangle\langle\chi_{1u}|\boldsymbol{\mu}_{10}^{e}\cdot\boldsymbol{\varepsilon}_0|\chi_{00}\rangle\,|\psi_1\rangle\\
&= \frac{i}{\hbar}\sqrt{\frac{\pi}{2}}\tilde{A}(\omega-\omega_{vert})\boldsymbol{\mu}_{10}^{e}(\boldsymbol{R})\cdot\boldsymbol{\varepsilon}_0|\psi_1\chi_{00}\rangle.
\end{aligned} \tag{9}$$

Hence, in the limit of an ultrashort pulse, the nuclear wavepacket formed on the excited state $|\psi_1\rangle$ is a copy of the original nuclear wavefunction χ_{00}, multiplied by the electronic transition dipole moment $\boldsymbol{\mu}_{10}^{e}(\boldsymbol{R})$ (Fig. 1B). We note that one could also invoke the Condon approximation, $\boldsymbol{\mu}_{10}^{e}(\boldsymbol{R})\cong\boldsymbol{\mu}_{10}^{e}(\boldsymbol{R}_{eq}^{0})$, where $\boldsymbol{\mu}_{10}^{e}(\boldsymbol{R}_{eq}^{0})$ is the electronic transition-dipole moment at the ground-state equilibrium geometry, owing to the presumably small variation of the electronic transition-dipole moment with nuclear positions.[*]

[*] Nonequilibrium vibrational wavepacket is formed even if one perturbs the system with CW laser field. A first example of such cases is given by a system promoted into a metastable (decaying) state with a finite lifetime τ. Such a situation occurs whenever the system is embedded in a continuum of states – the continuum can be vibrational (predissociation) or electronic (autoionization). If the energy separation corresponding to the lifetime $\frac{\hbar}{\tau}$ is larger than the energy separation between the states, we form a wavepacket rather than a stationary state. A

View Article Online
DOI: 10.1039/C8FD00088C

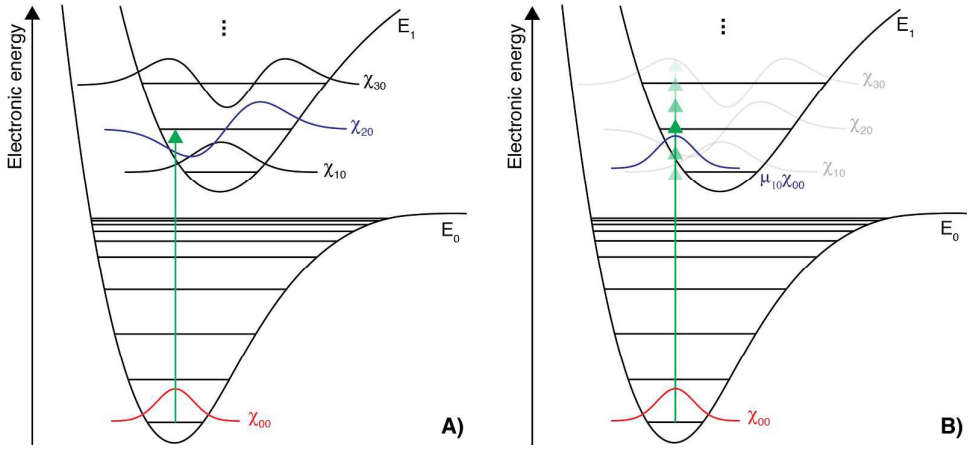

Figure 1. Sketch of different states formed upon the interaction of a molecule with laser field. (A) Interaction with CW laser, forming a stationary state (B) Interaction with ultrashort laser pulse, forming a wavepacket.

Semiclassical representation of the photoexcited states: Franck-Condon factor perspective

We further focus on a semiclassical representation of the vibrational states formed upon excitation with a laser field. Representing the wavepacket formed upon the interaction of a molecule with an ultrafast laser pulse is straightforward: we need to represent the ground state density by a set of atomic position and momenta and assign a weight of $|\boldsymbol{\mu}_{10}^{e}(\boldsymbol{R})|^2$ to each of the points. We comment on ways to achieve this goal below.

The situation is more difficult for the CW laser excitation as we rarely can model all of the possible final stationary states. Would we be able to do this, we would just analyze the properties of all the final states to get any of the observable quantities. However, the only easily available quantity is a single ground-state wavefunction or density. What is then the best classical representation of the final states formed upon the excitation? The analysis of Franck-Condon factors (FCFs) provides a clue.

We first assume one-dimensional system with an excited state exhibiting a dissociative character with a continuum of final vibrational states. We can linearize the excited potential energy surface along a classical turning point x_0 defined by the equation $E_f(x_0) - E_i(x_0) = E_{photon}$ (with E_f the energy of the final state and E_i that of the initial state)

vibrational wavepacket is also formed during photoemission processes with high-energy photons once we integrate the outcome over all energies of the outgoing electron.

View Article Online
DOI: 10.1039/C8FD00088C

$$E_f(x) = E_f(x_0) + E_f'(x_0)(x - x_0) + \cdots \tag{10}$$

Using energy normalization, the solution of Schrödinger equation for this potential is

$$\chi_f(E,x) \sim \left|E_f'(x_0)\right|^{-\frac{1}{2}} \mathrm{Ai}[a(x - x_0)] \,, \tag{11}$$

where Ai(x) stands for Airy function and $a = \left[\frac{2\mu E_f'(x_0)}{\hbar^2}\right]^{\frac{1}{3}}$. Replacing the Airy with δ function at the classical turning point

$$\chi_f(E,x) \sim \left|E_f'(x_0)\right|^{-\frac{1}{2}} \delta(x - x_0) \,, \tag{12}$$

yields FCF q_{fi} for the bound-to-free transition

$$q_{fi}(\chi_{iu}) \sim \left|E_f'(x_0)\right|^{-1} \chi_{iu}(x_0)^2 \tag{13}$$

which is equivalent to the exact FCF to the order a^{-2}. It is therefore reasonable to represent the scattering state by δ at a classical turning. The same FCF is equivalently achieved as

$$q_{fi}(E_{ph}, \chi_{iu}) \sim \int \chi_{iu}(x)^2 \delta\left(E_f(x_0) - E_0 - E_{ph}\right) dx \,. \tag{14}$$

This is in fact the reflection principle for the absorption cross section[22]: the nuclear density is reflected onto the excited state and further onto the energy axis. We end up with the same result in the time domain using a short time approximation for the propagator[23]. RP can be used therefore both for absorption cross-section estimates but also as a starting point for semiclassical molecular dynamics simulations. In the latter case, we just consider a particle starting from a classical turning point for a given photon energy. The RP is primarily designed for dissociative processes. However, it can also be used to approximate final bound excited state[22].*

The reflection integral can be generalized into multiple dimensions[24]:

* One can immediately see certain drawbacks of the reflection approximation outlined above. First, the real potential is not strictly linear, which however does not pose a problem if we evaluate an integral in Eqs. (15) or (16) numerically. A second problem arises from the approximation of the Airy function by a delta function, as this approximation will fail in areas with rapidly changing wavefunctions (e.g. at nodes) and especially at the wings of the distribution, where the third derivative of a wavefunction vanishes slower as compared to the wavefunction itself.

View Article Online
DOI: 10.1039/C8FD00088C

$$S_{fi}(E_{ph}, \varrho_i) \sim \int \varrho_i(\boldsymbol{R}) \left(\boldsymbol{\mu}_{fi}^e(\boldsymbol{R})\right)^2 \delta\left(E_f(\boldsymbol{R}) - E_i(\boldsymbol{R}) - E_{ph}\right) d\boldsymbol{R} \quad (15)$$

where $\boldsymbol{R}$ is the vector of nuclear coordinates, $\varrho_i(\boldsymbol{R})$ is the ground state coordinate density (the formula holds true even for mixed states). $S_{fi}(E_{ph}, \varrho_i)$ is called the intensity factor and, unlike FCF, includes a square of the transition-dipole moment. It is even more relevant to look at the expression for the intensity factor in the classical limit of the Fermi Golden rule in the Wigner representation[25]

$$S_{fi}(E_{ph}, P_T) \sim \int P_T(H_i(\boldsymbol{R}, \boldsymbol{P})) \left(\boldsymbol{\mu}_{fi}^e(\boldsymbol{R})\right)^2 \delta\left(H_f(\boldsymbol{R}, \boldsymbol{P}) - H_i(\boldsymbol{R}, \boldsymbol{P}) - E_{ph}\right) d\boldsymbol{R} d\boldsymbol{P} \quad (16)$$

where H_i and H_f are the classical Hamiltonians in the initial and final states and P_T is the thermal probability, factor which can be replaced by the nuclear density. The expression is in fact identical to (15), assuming processes in which momentum does not change. Note that in the multidimensional case we use energy resonance condition $E_f(\boldsymbol{R}) - E_i(\boldsymbol{R}) = E_{ph}$ rather than $E_f(\boldsymbol{R}) - E_0 = E_{ph}$ - while the latter expression approximate well the bound-unbound transition, the former expression represents a well-defined general approximation[26].

Despite its limitations, the reflection principle is pictorially appealing and it has been successfully applied for single and two photon spectroscopies[27], predissociation[28], imaging ground state vibrational wavefunctions[29–33] or extraction potentials from experimental data[34]. The approach can be extended to polyatomic molecules[24,35–38] and it is also the basis for the semiclassical initial condition selection. The approach is in fact known under different names, e.g. "nuclear ensemble method"[38] or δ-method[27].

Initial conditions for semiclassical simulations: short pulse

Armed with the theoretical background of the previous sections, we can now turn our attention to the central question how to properly choose the initial conditions for excited-state semiclassical MD simulations. As stated above, the answer to this question is relatively clear for the case of processes forming a nuclear wavepacket in the excited electronic state. To start a swarm of classical trajectories, we need to map the ground-state wavefunction or more generally density matrix onto a phase space. There are several ways in which one can formally perform this mapping[39], most famously with a Wigner transform of the initial vibrational wavefunction[40,41]

View Article Online
DOI: 10.1039/C8FD00088C

$$W(\boldsymbol{R},\boldsymbol{P}) = \frac{1}{(2\pi)^{3N}} \int_{-\infty}^{\infty} \chi_{iu}^{*}\left(\boldsymbol{R} + \frac{\hbar \boldsymbol{Q}}{2}\right) \chi_{iu}\left(\boldsymbol{R} - \frac{\hbar \boldsymbol{Q}}{2}\right) e^{i\boldsymbol{P}.\boldsymbol{Q}} d\boldsymbol{Q}\,, \tag{17}$$

where χ_{iu} is the initial vibrational wavefunction and N is the dimensionality of the configurational space. Quantum evolution of Wigner distribution is governed by a quantum Liouville operator and the semiclassical approach is recovered with corresponding classical Liouvillian[42]. Each classical trajectory sampled from the initial Wigner distribution should be weighted by a square of the electronic transition dipole moment $\boldsymbol{\mu}_{fi}^{e}(\boldsymbol{R})$. The Wigner function resembles a classical probability distribution function in the phase space, yet the function is generally not positive definite.[43] The evaluation of a Wigner function is generally also not straightforward for multidimensional anharmonic system and the Wigner approach is therefore typically used within the harmonic approximation. Here, the Wigner function is simply given as[23]

$$W(\boldsymbol{R},\boldsymbol{P}) = |\chi(\boldsymbol{R})|^2\, |\phi(\boldsymbol{P})|^2 \tag{18}$$

where $\chi(\boldsymbol{R})$ and $\phi(\boldsymbol{P})$ are the corresponding harmonic vibrational wavefunction in position and momentum representation, respectively. The evaluation of the Wigner transform is then easy within *ab initio* calculations using normal-mode frequencies, both in the ground state and at finite temperature[44]. However, harmonic approximation is problematic for soft normal modes, in practice below 500 cm^{-1} [45]. It is thus not at all clear what one should do for photodynamical simulations of liquids or in complex environments such as proteins.

The sampling of an approximate Wigner distribution for uncoupled harmonic oscillators is the most commonly employed strategy for trajectory trajectory-based simulations[14,46]. The simplicity of its construction, requiring only a frequency calculation at the ground-state equilibrium geometry, may explain the popularity of this approach. However, the deficiencies listed above, that is the lack of coupling between the modes and the neglect of anharmonicity, are particularly problematic for molecules and can lead to serious artifacts[46]. The use of classical *ab initio* molecular dynamics in the ground electronic state to generate initial conditions was questioned recently in the context of trajectory surface hopping method[14]. While this strategy adequately incorporates anharmonicities in the sampling, the classical treatment of the nuclear degrees of freedom implies that the resulting distribution at room temperature would correspond to an average energy substantially lower than the zero-point energy. In the context of QM/MM nonadiabatic dynamics, initial conditions have been obtained from an approximate Wigner sampling for the QM part and molecular dynamics for

View Article Online
DOI: 10.1039/C8FD00088C

the environment (MM part)[47]. Another strategy consists in sampling a classical Boltzmann[48] distribution using Brownian trajectories[49]. Recent works proposed to transform an approximate Wigner distribution to a more accurate one by performing an adiabatic switching[50,51]. This strategy was applied to different systems[52] but up to now it has not been used in the context of excited-state dynamics of molecules, to the best of our knowledge.

Density in coordinate space is efficiently sampled with path-integral molecular dynamics (PIMD) simulations[53]. Here each particle is represented by a ring polymer composed of "beads" or "random walkers" connected by "quantum forces". By increasing the number of the beads, the distribution of beads converges to the quantum distribution of a particle. The PIMD simulations were applied in the context of electronic spectroscopy for isolated molecules[54] and liquids[55,56] as well as for photodynamical simulations[57–59]. However, it is hard to retrieve the momentum distributions from PIMD simulations[60]. Another disadvantage of the PIMD method is its increased computational cost as compared to classical molecular dynamics.

Both of the above problems (computational cost and lack of momenta) are circumvented within a quantum thermostat approach based on the generalized Langevin equation (QT-GLE) introduced by Ceriotti et al[15,61]. The idea is based on widening classical distributions to match the quantum distributions. Both classical and quantum distribution are Gaussians for harmonic oscillator. Classical distribution is converted into the quantum one via frequency-dependent temperature

$$T^* = \frac{\hbar\omega}{2k_B}\coth\frac{\hbar\omega}{2k_BT} \quad . \tag{19}$$

Such an approach has been used already in the early days of semiclassical simulations for 1D potentials and empirically by artificially elevating the temperature even for multidimensional systems[62]. Even *ab initio* studies of liquid water tried to empirically account for quantum effects by elevating the temperature[63]. One needs, however, to maintain different temperatures for different normal modes, which is achieved with the Generalized Langevin equation (GLE) thermostat[15,61]. QT-GLE approach is exact for harmonic systems and provides a reasonable approximation even for anharmonic cases[61]. Importantly, the quantum thermostat approach also provides the distribution of momenta. Therefore, it makes a reasonable alternative to the harmonic Wigner approach for larger and moderately anharmonic systems. However, one should be aware of the potential ZPE leakage problem, in which the energy flows from high-frequency to low-frequency normal modes[64]. The reliability of the quantum-thermostat based

View Article Online
DOI: 10.1039/C8FD00088C

simulations can be tested by performing full PIMD simulations. Using novel schemes to accelerate the convergence of PIMD, such simulations are becoming routine.[65]

Initial conditions for semiclassical simulations: long pulse

Proper way of treating the simulation with a long laser pulse is to include the laser field into the simulation.[66–71] This is however not practical for excitations with weak fields as almost no transition would be then observed within duration of any realistic *ab initio* simulation.

We can solve the issue in the semiclassical framework by a proper choice of initial conditions. The photon energy is well-defined and we selectively populate only vibrational levels fulfilling a resonance condition

$$E_{ph} = E_{fu} - E_{iu}\,, \tag{20}$$

where E_{ph} is energy of the incident photon and E_{fu} stands for energy of the molecules in the u^{th} vibrational level of the f^{th} electronic state (the same notation applies for the energy of the initial state). We have seen above that we can assume the final state to be reasonably well represented by a δ function at a classical turning point. In practice, we sample the initial state density, *e.g.* by means of the MD simulations, and we assign each trajectory to a certain bin around a photon energy $E_{ph}(i)$. Within the spirit of reflection principle, we approximate

$$E_{fu} - E_{iu} = E_f(\boldsymbol{R}) - E_i(\boldsymbol{R}). \tag{21}$$

The practical realization of this strategy relies on running a swarm of trajectories sampled from the initial density, subject to the energy condition (Eq. (21)). The initial state is characterized by a distribution in a phase space reflecting the initial state of the system, in principle in thermal equilibrium. Let us assume that we use a Wigner distribution function. The CW laser then samples only a subspace of that distribution

$$\rho\big(\boldsymbol{R}, \boldsymbol{P}, E_{ph}\big) = W(\boldsymbol{R}, \boldsymbol{P})\delta\big(E_f(\boldsymbol{R}) - E_i(\boldsymbol{R}) - E_{ph}\big) \tag{22}$$

Note that we ignore kinetic energy contributions. The full distribution $W(\boldsymbol{R}, \boldsymbol{P})$ is generated by either explicitly calculating the wavefunction or by running MD simulations. In this work, we use the quantum-thermostat based MD method, which provides us with quantum distributions of positions and momenta. The filtering of the initial conditions was solved previously[72], yet not in a systematic manner.

View Article Online
DOI: 10.1039/C8FD00088C

Realization of the resonance condition: dynamics with constraints

In practice, we wish to select only the configurations from the MD simulation runs where the resonance condition is fulfilled within a predefined error. The straightforward approach based on running unconstrained dynamics then becomes impractical when the energy of the laser beam is set to the tail of the photoabsorption spectrum. We therefore apply strategies from accelerated dynamics or importance sampling to improve the efficiency of the simulations.

We consider here two techniques to guarantee the resonance condition: (*i*) methods of Lagrange multipliers (LM) and (*ii*) umbrella sampling[73–75].

We start with the LM approach, defining the holonomic constrain

$$\sigma_{\boldsymbol{R}}(t) = E_f(\boldsymbol{R}(t)) - E_i\big(\boldsymbol{R}(t)\big) - c = 0\,, \tag{23}$$

where constant $c = \hbar\omega$ is the photon energy. This leads to an additional force term in the classical equations of motion, which then read (for N atoms)

$$m_\gamma \frac{\partial^2 \boldsymbol{R}_\gamma(t)}{\partial t^2} = -\nabla_{\boldsymbol{R}_\gamma}\left[E\left(\boldsymbol{R}_\gamma(t)\right) + \lambda\sigma_{\boldsymbol{R}_\gamma}(t)\right], \qquad \gamma = 1 \ldots N \tag{24}$$

where the Lagrange multiplier λ is set in such a way that the constraint (Eq. (23)) is fulfilled. The equations of motion are (numerically) integrated

$$\boldsymbol{R}_\gamma(t+\Delta t) = \boldsymbol{R}^0_\gamma(t+\Delta t) + \lambda\nabla_{\boldsymbol{R}_\gamma}\sigma_{\boldsymbol{R}_\gamma}(t)(\Delta t)^2 m_\gamma^{-1}, \qquad \gamma = 1 \ldots N \tag{25}$$

where $\boldsymbol{R}^0$ is the position of the particles if no additional force were applied. The gradient of $\sigma_{\boldsymbol{R}}(t)$ is calculated as the difference between the gradients in the final and initial state. The holonomic constraint at time $t + \Delta t$ is expanded as

$$\sigma_{\boldsymbol{R}}(t+\Delta t) \cong \Delta E(t) + \frac{\partial \Delta E}{\partial \Delta \boldsymbol{R}}\Delta\boldsymbol{R}\,, \tag{26}$$

where ΔE represents a deviation from the target energy, $\Delta E = (E_f(\boldsymbol{R}) - E_i(\boldsymbol{R}) - c)$, and $\Delta\boldsymbol{R}$ is the change in positions $\Delta\boldsymbol{R} = \boldsymbol{R}(t+\Delta t) - \boldsymbol{R}(t)$, depending on λ. We wish the value of $\sigma_{\boldsymbol{R}}$ to remain zero. Using a stationarity condition for the Lagrangian $L(\boldsymbol{R},\lambda) = (E_f(\boldsymbol{R}) - E_i(\boldsymbol{R})) - \lambda\sigma_{\boldsymbol{R}}(t)$

$$\frac{\partial L(\boldsymbol{R},\lambda)}{\partial\lambda} = 0 - \sigma_{\boldsymbol{R}}(t+\Delta t) - \lambda\frac{\partial\sigma_{\boldsymbol{R}}(t+\Delta t)}{\partial\lambda} = 0 \tag{27}$$

we obtain:

View Article Online
DOI: 10.1039/C8FD00088C

$$\lambda = -\frac{\Delta E}{\sum_\gamma \left(\frac{\partial \sigma_{\boldsymbol{R}}(t)}{\partial \boldsymbol{R}_\gamma}\right)^2 \frac{\Delta t^2}{m_\gamma}} \,. \tag{28}$$

In the umbrella sampling approach, the system is forced to stay close to certain structures defined by a set of coordinates (collective variable, CV) *via* a restraining potential, but free to move in all remaining coordinates. The approach is routinely used for calculating free energy differences in classical molecular dynamics simulations[76,77]. In our case, the CV is not a direct combination of geometrical parameters. Instead, we define the CV via $\Delta E(\boldsymbol{R}) = E_f(\boldsymbol{R}) - E_i(\boldsymbol{R})$. The energy of both the initial and final electronic states depends on molecular geometries. We then choose a quadratic restraining potential in these coordinates such that the dynamics only samples the relevant part of the phase space for the selected excitation energy. The dynamics will then take place on a modified potential

$$\widetilde{E}_i(\boldsymbol{R}) = E_i(\boldsymbol{R}) + k\big(\Delta E(\boldsymbol{R}) - \Delta E_{target}\big)^2, \tag{29}$$

where k is the restraining force constant. To calculate forces acting on each atom, we need to know both the gradient in the ground state as well as the gradient in the excited state. This leads to an increase in computational cost, as excited-state methods are typically more time consuming compared to their ground-state counterparts. But even if one has to calculate excited-state energies at each step, the procedure is efficient for the tails of the distribution as the probability of reaching these structures without a bias decay exponentially with energy.

There are certain problems related to the coupling of importance sampling techniques with a thermostat. Classical thermostats are used without any further adaptation. On the contrary, the quantum thermostat "feels" the artificial force acting on the system to constrain the motion, recognizing the fast oscillations brought by the restraining force and will attempt to thermalize this degree of freedom as a quantum harmonic oscillator. Confining the position then leads to unphysical momenta generated in the system. We cope with the problem by constructing a quantum thermostat with damping[78] of artificial frequencies introduced by the Lagrangian dynamics.

Non-Condon effects in excited-state simulations

The transition dipole moment $\boldsymbol{\mu}_{if}^{e}(\boldsymbol{R})$ or associated oscillator strength $f_{if}(\boldsymbol{R})$ are not independent of molecular geometries and non-Condon effects can sometimes have profound effects on molecular spectra. As an example, the dissociation of nitrate anion never takes

View Article Online
DOI: 10.1039/C8FD00088C

place from structures close to the minimum ground-state geometry as the transition to the first excited band is forbidden at this molecular configuration[56]. To account for these non-Condon effects, we assign a weight to each trajectory so that any dynamical quantity $A(\boldsymbol{R}, \boldsymbol{P})$ is then calculated as

$$\langle A \rangle(t) = \sum_j w(\boldsymbol{R}_j^0) A\left(\boldsymbol{R}_j(t), \boldsymbol{P}_j(t)\right), \tag{30}$$

where $\boldsymbol{R}_j^0$ denotes the initial positions taken from the ground-state sampling (j runs over the sampled structures). In the present case, the quantity A is the kinetic energy of the outgoing chlorine fragment. The additional weight can reflect different electronic populations at each time. The weight factor is then given as

$$w(\boldsymbol{R}_j^0) = \frac{f_{if}(\boldsymbol{R}_j^0)}{\sum_k f_{if}(\boldsymbol{R}_k^0)} \ , \tag{31}$$

where the denominator is a normalization constant.

Test System: CF_2Cl_2 (Freon-12)

The CFCs absorb readily in the UV, producing chlorine radical, which catalyzes the well-known ozone decomposition[79]. Somewhat surprisingly, the photodissociation dynamics of these species is still not fully understood at the molecular level. The CF_2Cl_2 molecule starts to absorb UV photons around 205 nm, which is enough to dissociate the C-Cl bond

$$CF_2Cl_2 \rightarrow CF_2Cl + Cl$$

The absorption spectrum of CFC-12 peaks below 180 nm and the spectrum is rather narrow[80], with a half-width at half-maximum of less than 10 nm.

The photodissociation of the CF_2Cl_2 molecule was studied several times, always with laser frequencies on the red tail of the spectrum[81–86], with somewhat contradictory results. In the experiments by Baum and Huber[84] and Yen et al.[85], the chlorine fragment kinetic energy distributions were measured by TOF technique, using excitation laser with 193.3 nm[84] and 187 nm wavelength[85], respectively. While Baum and Huber observed only a single reaction channel characterized by a total kinetic energy (TKER) release of 1.475 eV,[84] Yen et al. observed also additional channels with the energy of 0.53 eV and 0.12 eV (together with the

View Article Online
DOI: 10.1039/C8FD00088C

main channel at TKER=1.63 eV)[85]. These two channels were tentatively assigned as fragments resulting from a second dissociation

$$CF_2Cl \rightarrow CF_2 + Cl$$

and formation of an excited-state CF_2Cl* fragment. More recently, the photodissociation dynamics was re-measured by Poterya et al.[87,88] at 193 nm using velocity map imaging technique. They found a dominant molecular peak at a chlorine fragment energy of 0.97 eV (corresponding to TKER=1.368 eV), but slower fragments were observed as well. On the other hand, the laser-induced fluorescence measurement of the quantum yield for the chlorine photodissocation was reported to be 1.03 at 193 nm, suggesting that only a single chlorine atom is dissociated.[86] In our work, we simulate the photodissociation dynamics at 193 nm. We compare our results to the most recent data of Poterya et al[87,88]. This test case was chosen as (*i*) enough high-quality experimental data are available, (*ii*) dynamical aspects are important as we need to find out the distribution of the excess energy between different fragments and (*iii*) simulations can answer the question whether double dissociation takes place.

Electronic structure

To describe bond dissociation, we need to cover the static correlation[89]. The simplest way is to use the complete active space self-consistent field method (CASSCF); we used even its cheaper alternative known as the Floating Occupation Molecular Orbitals CASSCI (FOMO-CASCI) method[90], which turned out to be an appealing alternative for the computational photodynamics[91]. The missing dynamical correlation could be added at the price of an increase in computational cost, e.g. with perturbative (CASPT2) or variational (MRCI) treatment. Here, we develop a simple empirical correction to obtain correct energetics in the dissociation limit. We start with the FOMO-CASCI energies and add an additional correlation energy correction (CEC). The correction is based on the assumption that the correlation contribution depends solely on the C-Cl bond distance and is independent of the electronic state. The imperfection of the FOMO-CASCI method is then manifested already at the ground state, yielding incorrect bond dissociation energies. We suggest a functional form to correct for the FOMO-CASCI deficiencies and tune the parameters against high-level *ab initio* calculations. The technical details of our approach are explained in the Supplementary Information.

The ground-state PES of CF_2Cl_2 was sampled at the B3LYP/6-31+g* level, since the B3LYP geometry matches the experiment. The energy constraint condition and subsequent excited-

View Article Online
DOI: 10.1039/C8FD00088C

state dynamics were performed using the FOMO-CASCI method with an active space of 12 electrons in 8 orbitals and a 6-31+g* basis sets[90]. The broadening parameter beta was set to 0.42 a.u. to obtain energies close to the reference CASSCF values.

Simulation details

We maintained a temperature of 200 K in the simulations, using a Nosé-Hoover thermostat for the classical simulations, or a quantum thermostat based on GLE for the simulations incorporating nuclear quantum effects[61]. GLE matrices were obtained from an online library[92] and were further modified to employ the so-called delta thermostat[78] in order to damp the high-frequency modes introduced by the additional constraints (additional details can be found in the SI). A time step of 20 a.u. was used for the MD sampling without any constraint, while a time step of 5 a.u. was employed in the constrained MD simulations to better conserve the resonance energy condition. The equations of motion were integrated using the velocity Verlet algorithm. The MD simulations were executed using a development version of the ABIN MD code[93], coupled either with the Gaussian 09[94] or GPU-accelerated TeraChem[95] electronic-structure codes. The photodynamical simulations were performed in the ABIN code coupled with the TeraChem.

Results and Discussion

The excitations of the CF_2Cl_2 molecule into its first 8 excited singlet states correspond to the promotion of an electron from a lone-pair (located on one of the chlorine atom) into one of the σ*(C-Cl) antibonding orbitals. The first excitation energy at the Franck Condon point is 7.26 eV (calculated at the EOM-CCSD/aug-cc-pVTZ level) and the second excited state of similar character is located only 0.30 eV above the first state. These values are close to the center of the first peak in the absorption spectrum.

Figure 3 shows the topography of the S_0 and S_1 PESs of the CF_2Cl_2 molecule, using the two C-Cl bond distances as reaction coordinates. The S_1 PES is purely repulsive with respect to both of the C-Cl bonds. The simultaneous dissociation of chlorine atoms is in principle energetically allowed, yet the process is not probable as we discuss below. We also see a non-smooth behavior at the $r(C\text{-}Cl_1) = r(C\text{-}Cl_2)$ line. The lack of differentiability originates from the crossings with the upper electronic states – the dissociation along the two C-Cl coordinates takes place on two diabatic surfaces crossing at the symmetric C_{2v} geometries.

View Article Online
DOI: 10.1039/C8FD00088C

Upon the excitation, the system should follow either one or the second valley, corresponding to the CF_2Cl + Cl products. The molecule is bound with respect to the C-F bonds in the first excited states. At the dissociation limit, three electronic states merge for the channel with a single dissociated chlorine atom, and nine states merge when both chlorine atoms are dissociated simultaneously. The degeneracy stems from the degeneracy of the atomic p-states of the free chlorine radicals. The potential energy scans including first 9 singlet states are shown in the Supplementary material.

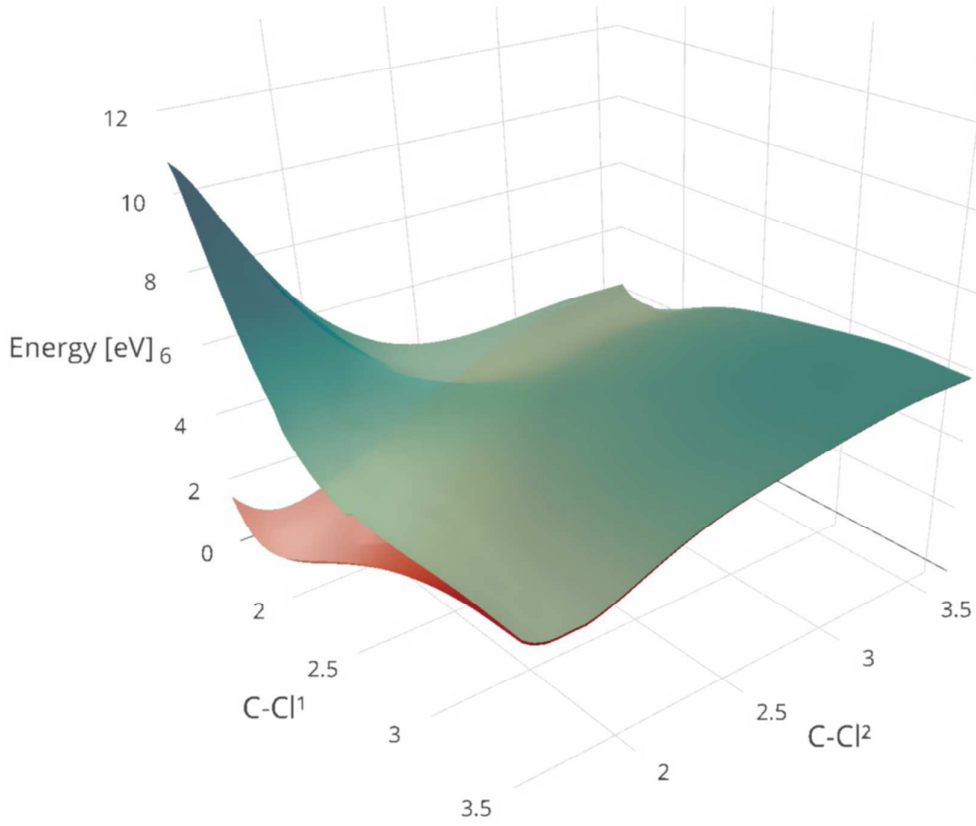

Figure 3. Scan of the S_0 and S_1 PESs of CF_2Cl_2 along the two dissociative C-Cl coordinates. The two electronic states were calculated at the FOMO-CASCI level, using an active space of 12 electrons in 8 orbitals and a 6-31+g* basis set.

The FOMO-CASCI PES is qualitatively reasonable, even if it does not provide a quantitative description of the system. The excitation energy is higher by ~1 eV and the asymptotic energetics is incorrect due to the lack of dynamical correlation. Figure 4 shows the ground-state potential energy curve along the C-Cl coordinate calculated at the FOMO-CASCI level, together with a corrected potential energy curve with the CEC correction. The correction is relatively large as it exceeds 1 eV.

View Article Online
DOI: 10.1039/C8FD00088C

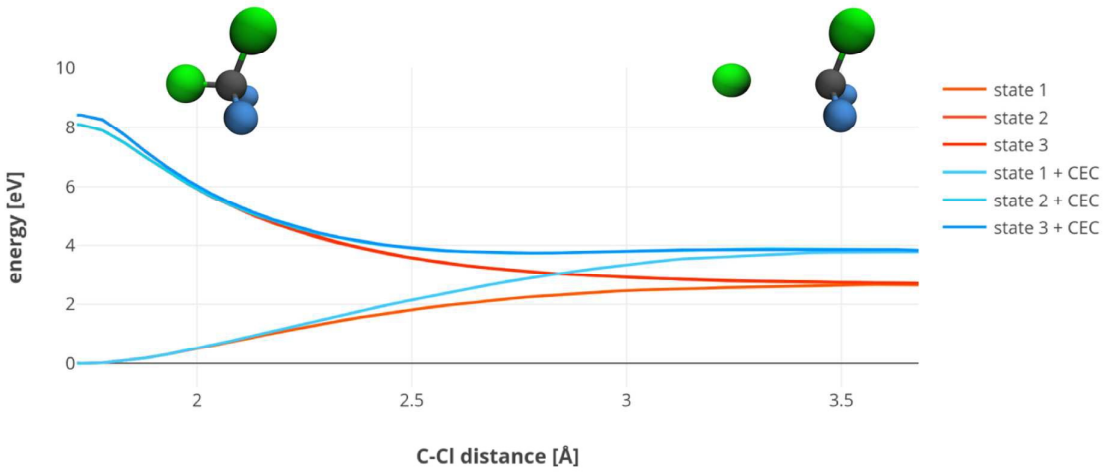

Figure 4. One-dimensional potential energy curves rigid scan of CF_2Cl_2 molecule calculated at the FOMO-CASCI level and compared with the corrected potential energy curves using the simple CEC empirical correction.

Let's now compare the ground-state energetics of the C-Cl bonds calculated with the FOMO-CASCI+CEC approach against the CCSD(T) calculations. For a dissociation of the single chlorine atom, CCSD(T) gives a dissociation energy of 3.59 eV, which compares well with the experimental value[96]. The FOMO-CASCI+CEC was fitted to match this value. The correction works, however, equally well for a double dissociation: here the CCSD(T) method predicts a dissociation energy of 5.60 eV, while FOMO-CASCI+CEC gives 5.55 eV.

Let us now focus on the proper sampling of the system in its ground state in the coordinate domain. Figure 5 shows the nuclear density along the two dissociative C-Cl coordinates in the ground-electronic state of the CF_2Cl_2 molecule. First, we can compare the quantum-thermostat generated density against the classical distribution. If no constraints are applied, the quantum distribution is significantly extended, reaching to C-Cl distances of 1.95 Å while the classical distribution essentially ends at a distance of 1.87 Å. It is also clearly seen that the data get sparser at the tail of the distribution, and we observe traces of particular trajectories. Quite different is the density distribution satisfying the energy resonance condition Eq. (21), *i.e.*, corresponding to semiclassical simulations with a constant wavelength. The selected points are all characterized by extended C-Cl distances. We also observe that the classical and quantum distributions do not differ too much in the present case – this is, however, only true for the coordinates strongly affecting the excitation energies, e.g. the densities along the C-F bonds are not influenced by the energy constraint to that extent.

View Article Online
DOI: 10.1039/C8FD00088C

In principle, we should worry about the non-ergodicity brought about by the energy constraint. Apparently, we did not face such an issue in the present simulations. Would we focus, however, on even longer excitation wavelengths, there might be only a small probability to sample points with both C-Cl bonds extended. The sampling would then not respect the symmetry of the problem – an issue that could be solved by running several independent sampling runs starting from an unconstrained simulation, for example.

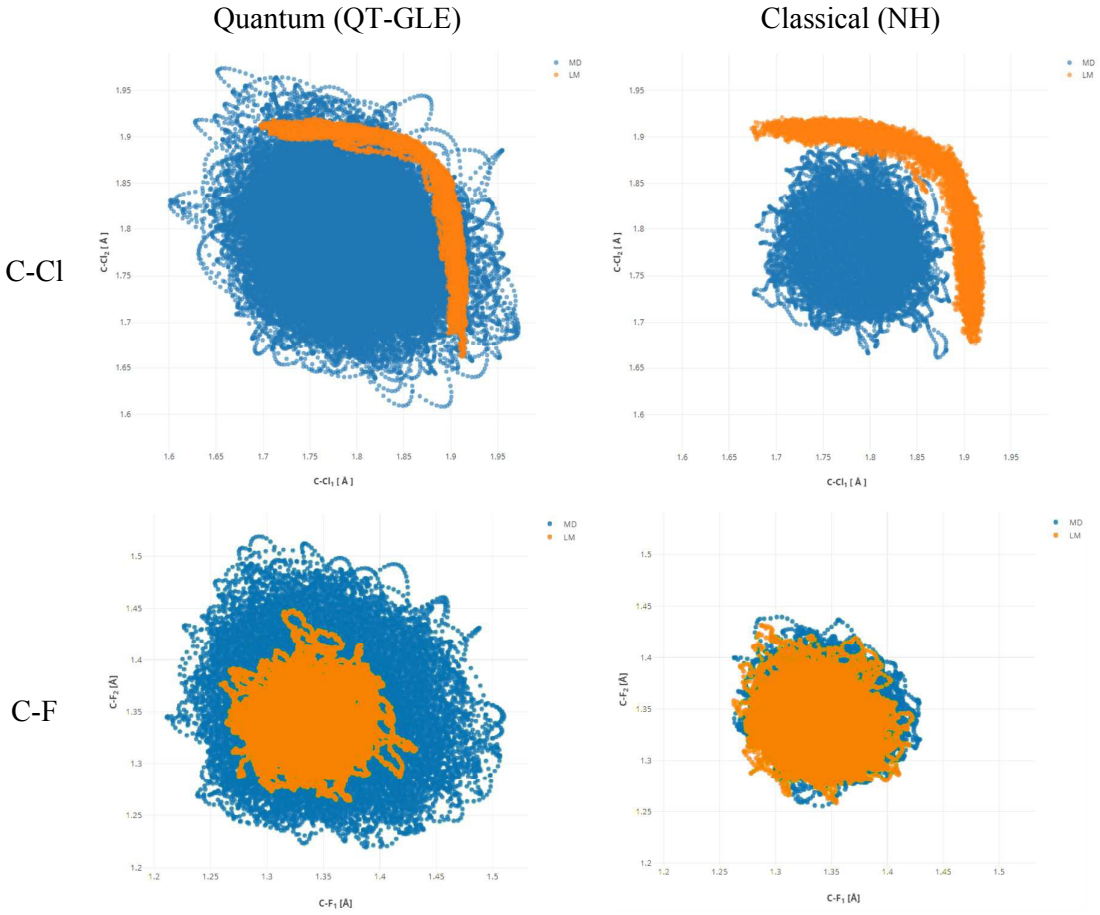

Figure 5. Ground-state density of the CF_2Cl_2 molecule plotted along the two C-Cl coordinates, governing the dissociation of the molecule. Panel A shows the results for the quantum thermostat, panel B shows the results for a Nosé-Hoover thermostat, *i.e.*, a classical distribution is generated. The points are generated along the MD trajectories lasting 100 ps. The orange points indicate simulations with the Lagrange multiplier constraints corresponding to the excitation wavelength of 193 nm. The ground-state PES was calculated at the FOMO-CAS-CI/6-31+g* level.

The relevance of the sampling is best visualized by a direct comparison of the excited-state simulation data with experiment. Here, we compare the kinetic energy distributions of the

View Article Online
DOI: 10.1039/C8FD00088C

outgoing chlorine atoms with the measurements at 193 nm obtained with the velocity map imaging approach[88]. The photodissociation of CF_2Cl_2 is an example of an almost direct photodissociation process. The molecule is excited on the steep second excited-state PES and one of the chlorine atoms immediately dissociates. The excess energy gets distributed among the kinetic energy of the chlorine atom and the remaining CF_2Cl molecular fragment. Most of the energy has been deposited into the fragment, especially in its internal degrees of freedom. Based on momentum conservation we can estimate the distribution ratio to be 2.31:1 for CF_2Cl : Cl. While the simulations were performed with the nonadiabatic surface hopping technique, the dynamics was overall essentially adiabatic. We could observe nonadiabatic transitions only during the latest stage of the reaction, essentially between degenerate electronic states. The second chlorine atom typically remained bound to the molecule within the duration of the simulations (200 fs) or scarcely dissociated after few vibrations of the remaining fragment. We did not observe an immediate double dissociation in a concerted fashion.

Figure 6A shows the resulting distribution of kinetic energies for simulations considering a vertical excitation. We always compare the simulations on the original FOMO-CASCI PESs against the simulations using the CEC modified PESs. The width of the spectrum is in both cases significantly narrower for the simulations starting from classical densities compared to the quantum distribution. Clearly, the zero-point energy allows for inspection of much more extended part of the coordinate space. The maximum of the KED for the FOMO-CASCI simulation is shifted by 0.8 eV up with respect to the experiment, *i.e.*, the chlorine fragments are almost twice as fast. We even observe a peak of slower chlorine atoms at around 0.6 eV, corresponding to the dissociation of the second chlorine atom. The second chlorine in this case dissociates almost simultaneously with the first atom. Application of the CEC correction makes, however, the fraction of the fast chlorine atoms seen in the direct photodissociation almost negligible. Furthermore, the center of the kinetic energy distribution shifts to 1.3 eV and it is now much closer to the experiment. However, the mean vertical excitation energy (that is, from the minimum ground state geometry) at the FOMO-CASCI level is almost 8 eV, *i.e.*, much larger than the experimentally used value of 6.43 eV. We also observe that the width of the KED peak is larger than the one seen in the experiment, the FWHM is 0.60 eV for the QT-GLE simulations while it is only 0.35 eV in the experiment.

View Article Online
DOI: 10.1039/C8FD00088C

We achieve an almost quantitative agreement with the experiment when the QT-GLE thermostat is coupled with the Lagrange multipliers to ensure the resonance conditions (Eq. (21)). Figure 6B show the spectrum calculated using the QT-GLE thermostat the CEC for energy constraints (*i*) 6.43 eV (193 nm) and (*ii*) 7 eV (close to the experimental maximum of absorption). For comparison, the 6.43 eV simulation results are also shown for classical MD sampling. The 6.43 eV QT-GLE simulation faithfully describes the KED of the chlorine atoms in the fast peak. The energy maximum of the peak at around 0.97 eV as well as the FWHM 0.37 eV are almost the same as the experimental values (0.98 eV and 0.35 eV, respectively). The 7 eV simulation is shifted to larger energy values while the width of the spectrum remains approximately correct. The classical spectrum is almost as wide as the quantum one. This contrasts with the spectrum for the vertical wavepacket simulation. Clearly, the energy condition (21) mitigates the quantum delocalization in the position space.

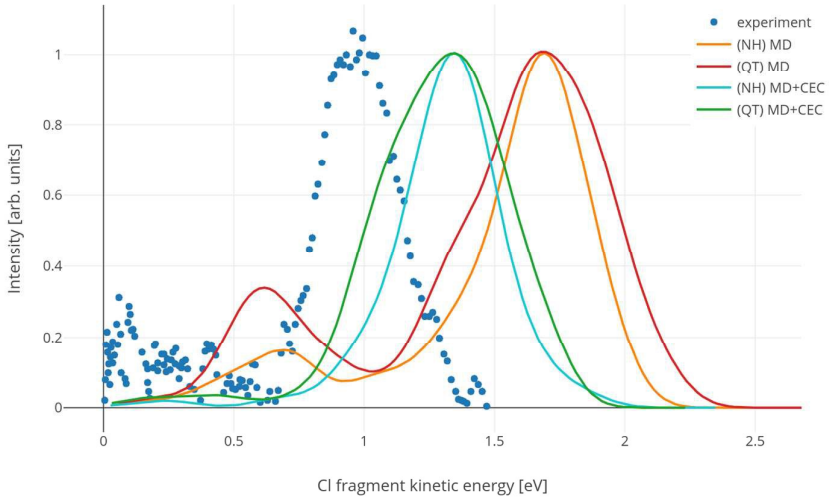

View Article Online
DOI: 10.1039/C8FD00088C

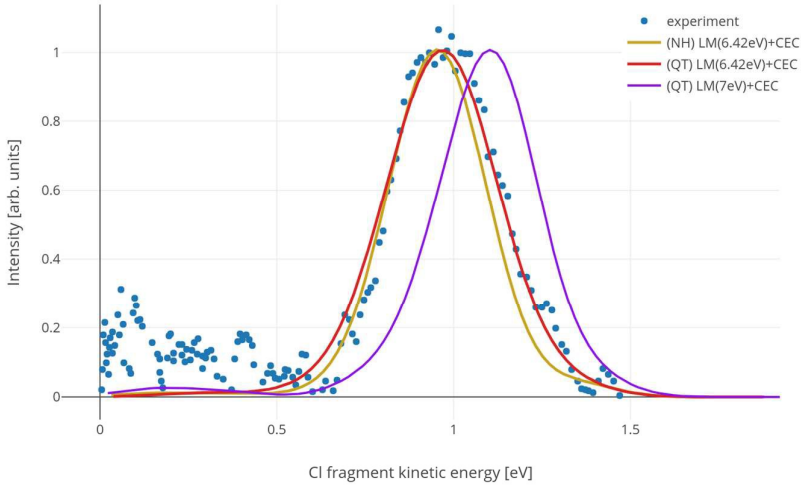

Figure 6. Kinetic energy distributions calculated with initial conditions corresponding to Figure 5, using either direct FOMO-CASCI or the FOMO-CASCI+CEC PESs. Upper panel shows the results for unconstrained simulations (corresponding to vertical excitations), lower panel shows the results with the resonance condition (21) imposed by means of Lagrange multipliers technique. Experimental data corresponding to a nanosecond laser pulse of 193 nm is showed for comparison[88].

Next, we briefly focus on the importance of the non-Condon effects in the simulations, that is, on the importance of weighting the simulations by the square of transition dipole moments or oscillatory strength (see Eq. (9)). Figure 7 shows the resulting KEDs for simulations at various conditions (differing by the underlying PES or by using imposing the resonance condition). We observe that the effect can be very larger. In particular, the quantum simulation on the FOMO-CAS-CI PES shows a profound effect of the non-Condon effects for the peak corresponding to slower chlorine atoms at around 0.5 eV. These chlorine atoms result from structures with both chlorine atoms partially dissociated already from the start of the simulations. Such arrangement has, however, lower probability when we consider the $\boldsymbol{R}$-dependence of the electronic transition dipole moment, *i.e.*, the functions $\boldsymbol{\mu}_{if}^{e}(\boldsymbol{R}) \cdot \boldsymbol{\varepsilon}_0 |\psi_f \chi_{iu}\rangle$ and $|\psi_f \chi_{iu}\rangle$ are quite different. The densities generated with the Lagrange-multiplier modified MD do not differ – in fact, this is consistent with the view that a single stationary state should be generated within the constant wavelength simulations.

View Article Online
DOI: 10.1039/C8FD00088C

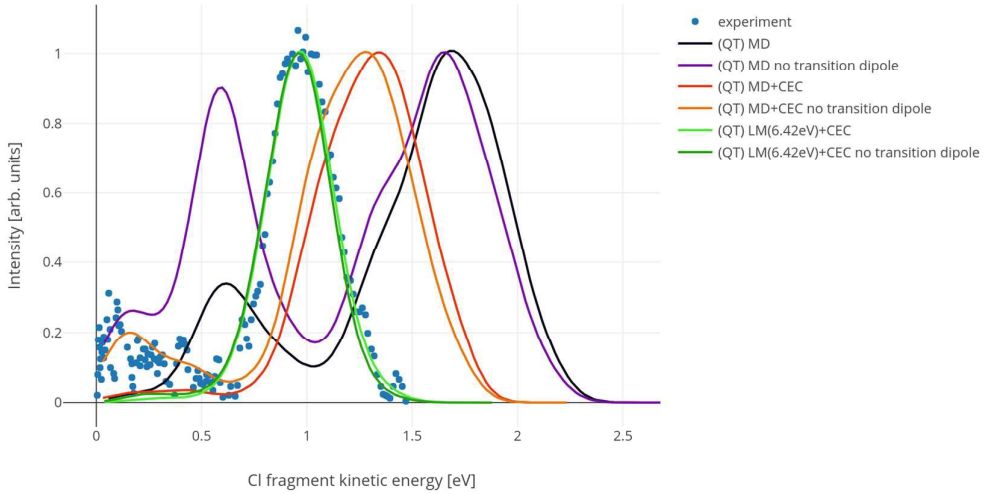

Figure 7. The role of non-Condon effects on the calculated distribution of chlorine kinetics energies upon photodissociation of CF_2Cl_2 with a nanosecond 193 nm laser pulse.

We obtained the data presented in the graphs above directly by analysis of the MD trajectories, *i.e.*, we focused only on the chlorine atoms leaving the clusters immediately within the duration of the MD simulations. The best simulations considering both the experimental laser wavelength and CEC correction for the FOMO-CASCI PES were, however, not able to reproduce the appearance of the slow chlorine atoms with near zero kinetic[85,87]. The origin of these chlorine atoms is not entirely clear. It has been hypothesized that they can result from concerted dissociation of the two Cl atoms, secondary dissociation of the CF_2Cl radical or two photon processes[87,88]. Here we assume that they result from statistical dissociation of the CF_2Cl radical formed within the direct photodissociation. We can estimate the excess energy E_{exc} deposited as an internal energy of the fragment knowing the dissociation energy of the C-Cl bond in the CFC-12 E_{C-Cl} and kinetic energy of the first chlorine atom $E_{kin,Cl}$

$$E_{exc} = E_{ph} - E_{C-Cl} - E_{kin,Cl} - E_{kin,CF_2Cl} + \Delta ZPE\ , \qquad (32)$$

where the kinetic energy of the CF_2Cl radical is estimated from momentum conservation and the ΔZPE correction accounts for different zero point energies of the products and reactants. We can then estimate the kinetic energy distribution of the second chlorine radical by means of statistical theory, using a simple formula[97]

View Article Online
DOI: 10.1039/C8FD00088C

$$P(E_{exc}, \epsilon_k) \propto \Omega(E_{exc} - \epsilon_k)\sqrt{\epsilon_k} \ , \tag{33}$$

where ϵ_k is the kinetic energy of the outgoing fragment, that is, the probability is proportional to the density of states of the chlorine atom and the density of states of the remaining fragment. In most cases, the dissociation of the second chlorine atom is not energetically available. However, the fraction of simulation with the lowest kinetic energy of the first chlorine atom allows for the dissociation of the second one. As a result, the total KED spectrum based on the combination of the MD simulations with statistical description of the fragment nicely fits the experiment (Figure 8). The fraction of chlorine atoms amounts to some 16% of the total chlorine population in the experiment, in a reasonable agreement with the calculated value of 8%.

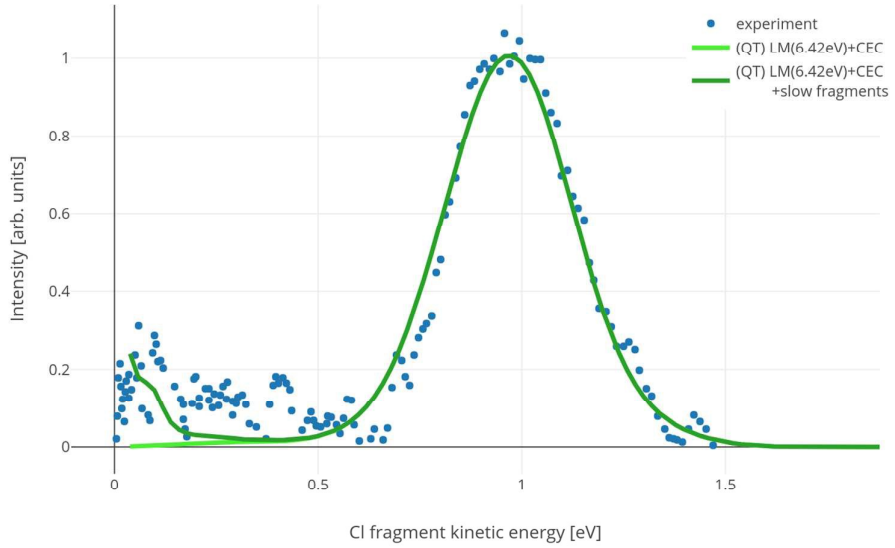

Figure 8. Simulations of the CF_2Cl_2 photodissociation on the FOMO-CASCI+CEC PESs including the slow chlorine atoms.

Conclusions

Semiclassical excited-state simulations are powerful as a tool for the investigation of photochemical processes. However, the contact with experiment is often imperfect – we gain insight, but not the numbers.

View Article Online
DOI: 10.1039/C8FD00088C

Here, we highlight two main problems in semiclassical excited-state simulations. (*i*) *Electronic structure theory*. Independent of the nonadiabatic scheme used, we can hardly get any reliable result with inadequate PESs – this aspect is widely acknowledged[2,3]. The problem is a limited choice of the techniques describing global PESs in the excited states. Two frequently used approaches suffer from known deficiencies: the TDDFT method lacks the ability to describe dissociation processes while CASSCF method is quantitatively inaccurate. In the present work, we show that the latter problem can sometimes be mitigated in a thrifty way, e.g. using the CEC potential introduced in this work. The correction is similar in spirit to two recently introduced (semi)empirical corrections to the CAS type wavefunctions. In the α-CASSCF method[98], a single empirical scaling factor is used to correct the CASSCF excitation energies. Hohenstein e*t al* proposed a simple DFT-based correction to CASCI energies and showed that this approach can remove spurious barriers on excited state energy surfaces[99]. (*ii*) *Selection of initial conditions*. One should always carefully consider what are the quantum states formed upon photoexcitation. We have advocated the use of the QT-GLE thermostat for the generation of initial conditions in the phase space for MD simulations. However, the present example did not fully benefit from the strength of the approach, as CF_2Cl_2 is a fairly harmonic system dissociating on a steep excited-state PES. The approach is indeed very general, and the QT-GLE strategy can easily be used for liquids or for processes where momentum distribution plays a decisive role. Most of the work focused on a proper way of treating excitations with a long laser pulse. We introduce a new technique to sample the initial state for such situations based on constrained dynamics in the ground state, demonstrating its performance on the example of the CF_2Cl_2 photodissociation.

The sampling of the initial state based on the enforcement of the energy resonance condition is computationally more demanding compared to a pure sampling of the ground-state vibrational wavefunction. Indeed, we have to sacrifice the appealing division of the simulation into two completely independent parts: sampling in the ground state, followed by excited-state dynamics. In our approach, we need to know the excited-state energies and forces already for the preparation of initial conditions, and the large excited-state forces impose a shortening of the time step. Alternatively, one could directly apply the energetic criterion to the distribution generated by the quantum thermostat or similar technique. The latter approach will be more efficient for excitation wavelengths close to the absorption maximum.

View Article Online
DOI: 10.1039/C8FD00088C

Next, we showed in our work that non-Condon effects, often neglected in excited-state photodynamical simulations, have in some situations a profound effect on the final observable quantities. We also combined the photodynamical simulations with statistical methods describing the dissociation of molecules in later stages of the reaction.

Extensions of the present computational protocol would be desirable. First, the CW-sampling method was introduced so far for a single excited state only. If more states are present, we could run the sampling independently for each of them. Alternatively, we could allow for excited-state jumps during the initial state sampling stage. The probability of transitions would now depend on the oscillator strengths of the respective states. Next, we might wish to simulate a system subjected to a pulse of general shape, or to an excited state with a certain finite lifetime. In this case, the wavepacket would not directly copy the ground-state distribution, and the umbrella sampling technique should be able to accommodate such situations.

Conflicts of interest

There are no conflicts to declare.

Acknowledgments

We gratefully acknowledge the financial support of Czech Science Foundation (project number 18-23756S). D. H. is a student of the International Max Planck Research School "Many-Particle Systems in Structured Environments".

View Article Online
DOI: 10.1039/C8FD00088C

References

1 D. Roca-Sanjuán, F. Aquilante and R. Lindh, *Wiley Interdiscip. Rev. Comput. Mol. Sci.*, 2012, **2**, 585–603.

2 F. Plasser, M. Barbatti, A. J. A. Aquino and H. Lischka, *Theor. Chem. Acc.*, 2012, **131**, 1073–1086.

3 L. González, D. Escudero and L. Serrano-Andrés, *ChemPhysChem*, 2012, **13**, 28–51.

4 J. W. Snyder Jr, B. F. E. Curchod and T. J. Martínez, *J. Phys. Chem. Lett.*, 2016, **7**, 2444–2449.

5 A. K. Belyaev, W. Domcke, C. Lasser and G. Trigila, *J. Chem. Phys.*, 2015, **142**, 104307.

6 M. Barbatti, *Wiley Interdiscip. Rev. Comput. Mol. Sci.*, 2011, **1**, 620–633.

7 J. C. Tully, *J. Chem. Phys.*, 1990, **93**, 1061–1071.

8 M. Ben-Nun and T. J. Martínez, *J. Chem. Phys.*, 1998, **108**, 7244–7257.

9 M. Ben-Nun, J. Quenneville and T. J. Martínez, *J. Phys. Chem. A*, 2000, **104**, 5161–5175.

10 B. F. E. Curchod and T. J. Martínez, *Chem. Rev.*, 2018, **118**, 3305–3336.

11 G. A. Worth, M. A. Robb and B. Lasorne, *Mol. Phys.*, 2008, **106**, 2077–2091.

12 D. V Shalashilin, *Faraday Discuss.*, 2011, **153**, 105–116.

13 S. K. Min, F. Agostini, I. Tavernelli and E. K. U. Gross, *J. Phys. Chem. Lett.*, 2017, **8**, 3048–3055.

14 M. Barbatti and K. Sen, *Int. J. Quantum Chem.*, 2016, **116**, 762–771.

15 M. Ceriotti, G. Bussi and M. Parrinello, *Phys. Rev. Lett.*, 2009, **103**, 030603.

16 P. Slavíček and M. Fárník, *Phys. Chem. Chem. Phys.*, 2011, **13**, 12123–12137.

17 R. J. Salter, M. A. Blitz, D. E. Heard, T. Kovács, M. J. Pilling, A. R. Rickard and P. W. Seakins, *Phys. Chem. Chem. Phys.*, 2013, **15**, 4984–4994.

18 A. Lauer, D. E. Fast, J. Steinkoenig, A.-M. Kelterer, G. Gescheidt and C. Barner-Kowollik, *ACS Macro Lett.*, 2017, **6**, 952–958.

19 B. Dietzek, S. Fey, R. A. Matute, L. González, M. Schmitt, J. Popp, A. Yartsev and G. Hermann, *Chem. Phys. Lett.*, 2011, **515**, 163–169.

20 V. Barone, M. Biczysko and C. Puzzarini, *Acc. Chem. Res.*, 2015, **48**, 1413–1422.

21 M. Persico, *Excited State Dynamics*, Universitá di Pisa, Madrid, 2007.

22 E. A. Gislason, *J. Chem. Phys.*, 1973, **58**, 3702–3707.

23 R. Schinke, *Photodissociation Dynamics: Spectroscopy and Fragmentation of Small Polyatomic Molecules*, Cambridge University Press, Cambridge, 1993.

View Article Online
DOI: 10.1039/C8FD00088C

24 F. Della Sala, R. Rousseau, A. Görling and D. Marx, *Phys. Rev. Lett.*, 2004, **92**, 183401.

25 B. Segev, *J. Opt. B Quantum Semiclassical Opt.*, 2003, **5**, S381.

26 J. Vaníček and D. Cohen, *Philos. Trans. R. Soc. A Math. Phys. Eng. Sci.*, 2015, **374**, 20150164.

27 P. Baierl and W. Kiefer, *J. Chem. Phys.*, 1982, **77**, 1693–1700.

28 A. D. Bandrauk and J.-P. Laplante, *Can. J. Chem.*, 1977, **55**, 1333–1341.

29 S. Chelkowski, P. B. Corkum and A. D. Bandrauk, *Phys. Rev. Lett.*, 1999, **82**, 3416–3419.

30 S. Chelkowski and A. D. Bandrauk, *Phys. Rev. A*, 2002, **65**, 23403.

31 L. P. H. Schmidt, T. Jahnke, A. Czasch, M. Schöffler, H. Schmidt-Böcking and R. Dörner, *Phys. Rev. Lett.*, 2012, **108**, 73202.

32 S. Zeller, M. Kunitski, J. Voigtsberger, A. Kalinin, A. Schottelius, C. Schober, M. Waitz, H. Sann, A. Hartung, T. Bauer, M. Pitzer, F. Trinter, C. Goihl, C. Janke, M. Richter, G. Kastirke, M. Weller, A. Czasch, M. Kitzler, M. Braune, R. E. Grisenti, W. Schöllkopf, L. P. H. Schmidt, M. S. Schöffler, J. B. Williams, T. Jahnke and R. Dörner, *Proc. Natl. Acad. Sci.*, 2016, **113**, 14651–14655.

33 K. Kwon and A. Moscowitz, *Phys. Rev. Lett.*, 1996, **77**, 1238–1241.

34 M. S. Child, H. Essén and R. J. Le Roy, *J. Chem. Phys.*, 1983, **78**, 6732–6740.

35 L. Šištík, M. Ončák and P. Slavíček, *Phys. Chem. Chem. Phys.*, 2011, **13**, 11998–12007.

36 S. Y. Lee, R. C. Brown and E. J. Heller, *J. Phys. Chem.*, 1983, **87**, 2045–2053.

37 S. Lee, *J. Chem. Phys.*, 1982, **76**, 3064–3074.

38 R. Crespo-Otero and M. Barbatti, *Theor. Chem. Acc.*, 2012, **131**, 1237.

39 H.-W. Lee, *Phys. Rep.*, 1995, **259**, 147–211.

40 E. Wigner, *Phys. Rev.*, 1932, **40**, 749–759.

41 M. Hillery, R. F. O'Connell, M. O. Scully and E. P. Wigner, *Phys. Rep.*, 1984, **106**, 121–167.

42 R. C. Brown and E. J. Heller, *J. Chem. Phys.*, 1981, **75**, 186–188.

43 W. Schleich, *Quantum optics in phase space.*, Wiley-VCH, Berlin, 2001.

44 E. J. Heller, *J. Chem. Phys.*, 1976, **65**, 1289–1298.

45 M. Ončák, P. Slavíček, M. Fárník and U. Buck, *J. Phys. Chem. A*, 2011, **115**, 6155–6168.

46 M. Persico and G. Granucci, *Theor. Chem. Acc.*, 2014, **133**, 1526.

View Article Online
DOI: 10.1039/C8FD00088C

47 M. Ruckenbauer, M. Barbatti, T. Müller and H. Lischka, *J. Phys. Chem. A*, 2010, **114**, 6757–6765.

48 P. Cattaneo, G. Granucci and M. Persico, *J. Phys. Chem. A*, 1999, **103**, 3364–3371.

49 T. Cusati, G. Granucci and M. Persico, *J. Am. Chem. Soc.*, 2011, **133**, 5109–5123.

50 A. Bose and N. Makri, *J. Chem. Phys.*, 2015, **143**, 114114.

51 C. Qu and J. M. Bowman, *J. Phys. Chem. A*, 2016, **120**, 4988–4993.

52 T. Nagy and G. Lendvay, *J. Phys. Chem. Lett.*, 2017, **8**, 4621–4626.

53 M. Tuckerman, *Statistical Mechanics: Theory and Molecular Simulation*, Oxford University Press, Oxford [England]; New York, 2010.

54 M. Ončák, L. Šištík and P. Slavíček, *J. Chem. Phys.*, 2010, **133**, 174303.

55 D. Hollas, E. Muchová and P. Slavíček, *J. Chem. Theory Comput.*, 2016, **12**, 5009–5017.

56 O. Svoboda, L. Kubelová and P. Slavíček, *J. Phys. Chem. A*, 2013, **117**, 12868–12877.

57 D. Hollas, O. Svoboda and P. Slavíček, *Chem. Phys. Lett.*, 2015, **622**, 80–85.

58 O. Svoboda, D. Hollas, M. Oncak and P. Slavicek, *Phys. Chem. Chem. Phys.*, 2013, **15**, 11531–11542.

59 J. Chalabala and P. Slavicek, *Phys. Chem. Chem. Phys.*, 2016, **18**, 20422–20432.

60 J. A. Morrone, V. Srinivasan, D. Sebastiani and R. Car, *J. Chem. Phys.*, 2007, **126**, 234504.

61 M. Ceriotti, G. Bussi and M. Parrinello, *J. Chem. Theory Comput.*, 2010, **6**, 1170–1180.

62 V. Lukeš, R. Šolc, M. Barbatti, H. Lischka and H.-F. Kauffmann, *J. Theor. Comput. Chem.*, 2010, **9**, 249–263.

63 R. A. DiStasio, B. Santra, Z. Li, X. Wu and R. Car, *J. Chem. Phys.*, 2014, **141**, 84502.

64 F. Brieuc, Y. Bronstein, H. Dammak, P. Depondt, F. Finocchi and M. Hayoun, *J. Chem. Theory Comput.*, 2016, **12**, 5688–5697.

65 T. E. Markland and M. Ceriotti, *Nat. Rev. Chem.*, 2018, **2**, 0109.

66 R. Mitrić, J. Petersen and V. Bonačić-Koutecký, *Phys. Rev. A*, 2009, **79**, 53416.

67 G. A. Jones, A. Acocella and F. Zerbetto, *J. Phys. Chem. A*, 2008, **112**, 9650–9656.

68 M. Richter, P. Marquetand, J. González-Vázquez, I. Sola and L. González, *J. Chem. Theory Comput.*, 2011, **7**, 1253–1258.

69 B. Mignolet, B. F. E. Curchod and T. J. Martínez, *J. Chem. Phys.*, 2016, **145**, 191104.

70 I. Tavernelli, B. F. E. Curchod and U. Rothlisberger, *Phys. Rev. A*, 2010, **81**, 52508.

71 J. J. Bajo, G. Granucci and M. Persico, *J. Chem. Phys.*, 2014, **140**, 44113.

View Article Online
DOI: 10.1039/C8FD00088C

72 P. Slavíček, P. Jungwirth, M. Lewerenz, N. H. Nahler, M. Fárník and U. Buck, *J. Phys. Chem. A*, 2003, **107**, 7743–7754.

73 T. Laino and D. Passerone, *Chem. Phys. Lett.*, 2004, **389**, 1–6.

74 T. Mori and T. J. Martínez, *J. Chem. Theory Comput.*, 2013, **9**, 1155–1163.

75 Y. Lei, S. Wu, C. Zhu, Z. Wen and S.-H. Lin, *Int. J. Photoenergy*, 2014, **2014**, 1–18.

76 G. M. Torrie and J. P. Valleau, *J. Comput. Phys.*, 1977, **23**, 187–199.

77 T. W. Allen, O. S. Andersen and B. Roux, *Biophys. Chem.*, 2006, **124**, 251–267.

78 J. A. Morrone, T. E. Markland, M. Ceriotti and B. J. Berne, *J. Chem. Phys.*, 2011, **134**, 14103.

79 F. S. Rowland and M.J. Molina, *Nature*, 1974, **249**, 810–812.

80 H. Keller-Rudek, G. K. Moortgat, R. Sander and R. Sörensen, *Earth Syst. Sci. Data*, 2013, **5**, 365–373.

81 R. E. Rebbert and P. J. Ausloos, *J. Photochem.*, 1975, **4**, 419–434.

82 J. J. Tiee, F. B. Wampler and W.-W. Rice, *Chem. Phys. Lett.*, 1979, **68**, 403–406.

83 Y. Matsumi, K. Tonokura, M. Kawasaki, G. Inoue, S. Satyapal and R. Bersohn, *J. Chem. Phys.*, 1991, **94**, 2669–2674.

84 G. Baum and J. R. Huber, *Chem. Phys. Lett.*, 1993, **203**, 261–264.

85 M. Yen, P. M. Johnson and M. G. White, *J. Chem. Phys.*, 1993, **99**, 126–139.

86 F. Taketani, K. Takahashi and Y. Matsumi, *J. Phys. Chem. A*, 2005, **109**, 2855–2860.

87 V. Poterya, J. Kočišek, A. Pysanenko and M. Fárník, *Phys. Chem. Chem. Phys.*, 2014, **16**, 421–429.

88 V. Poterya, J. Kočišek, J. Lengyel, P. Svrčková, A. Pysanenko, D. Hollas, P. Slavíček and M. Fárník, *J. Phys. Chem. A*, 2014, **118**, 4740–4749.

89 D. P. Tew, W. Klopper and T. Helgaker, *J. Comput. Chem.*, 2007, **28**, 1307–1320.

90 P. Slavíček and T. J. Martínez, *J. Chem. Phys.*, 2010, **132**, 234102.

91 D. Hollas, L. Šištík, E. G. Hohenstein, T. J. Martínez and P. Slavíček, *J. Chem. Theory Comput.*, 2017, **14**, 339–350.

92 GLE4MD input library, http://gle4md.org, (accessed 1 May 2018).

93 D. Hollas, J. Suchan, O. Svoboda, M. Ončák and P. Slavíček, ABIN, https://doi.org/10.5281/zenodo.1228462, 2018.

94 M. J. Frisch, G. W. Trucks, H. B. Schlegel, G. E. Scuseria, M. A. Robb, J. R. Cheeseman, G. Scalmani, V. Barone, B. Mennucci, G. A. Petersson, H. Nakatsuji, M. Caricato, X. Li, H. P. Hratchian, A. F. Izmaylov, J. Bloino, G. Zheng, D. J. Sonnenberg, M. Hada, M. Ehara, K. Toyota, R. Fukuda, J. Hasegawa, M. Ishida, T. Nakajima, Y. Honda, O. Kitao, H. Nakai, T. Vreven, J. Montgomery, J. A., J. E. Peralta, F. Ogliaro,

View Article Online
DOI: 10.1039/C8FD00088C

M. Bearpark, J. J. Heyd, E. Brothers, K. N. Kudin, V. N. Staroverov, R. Kobayashi, J. Normand, K. Raghavachari, A. Rendell, J. C. Burant, S. S. Iyengar, J. Tomasi, M. Cossi, N. Rega, J. M. Millam, M. Klene, J. E. Knox, J. B. Cross, V. Bakken, C. Adamo, J. Jaramillo, R. Gomperts, R. E. Stratmann, O. Yazyev, A. J. Austin, R. Cammi, C. Pomelli, J. W. Ochterski, R. L. Martin, K. Morokuma, V. G. Zakrzewski, G. A. Voth, P. Salvador, J. J. Dannenberg, S. Dapprich, A. D. Daniels, Ö. Farkas, J. B. Foresman, J. V. Ortiz, J. Cioslowski and D. J. Fox, *Gaussian, Inc. Wallingford CT*, 2013, 09.

95 I. S. Ufimtsev and T. J. Martinez, *J. Chem. Theory Comput.*, 2009, **5**, 2619–2628.

96 Y. L. Yung and W. B. DeMore, *Photochemistry of planetary atmospheres*, Oxford University Press, New York, 1999.

97 J. Laskin and C. Lifshitz, *J. mass Spectrom.*, 2001, **36**, 459–478.

98 J. W. Snyder, R. M. Parrish and T. J. Martínez, *J. Phys. Chem. Lett.*, 2017, **8**, 2432–2437.

99 S. Pijeau and E. G. Hohenstein, *J. Chem. Theory Comput.*, 2017, **13**, 1130–1146.